P wave Teleseismic Tomography of the Subducted Chile Rise

Matthew Miller[a,*], Keith Priestley[b], Frederik Tilmann[c,d], Klaus Bataille[e], Hikaru Iwamori[f]

[a]*Departamento de Geofísica, Universidad de Concepción, Concepción, Chile*
[b]*Department of Earth Sciences, Bullard Laboratories, University of Cambridge, Cambridge, United Kingdom*
[c]*Department of Geophysics, Deutsches GeoForschungsZentrum GFZ, Potsdam, Germany*
[d]*Department of Earth Sciences, Institute of Geological Sciences, Freie Universität Berlin, Berlin, Germany*
[e]*Departamento de Ciencias de la Tierra, Universidad de Concepción, Concepción, Chile*
[f]*Earthquake Research Institute, University of Tokyo, 1-1-1, Yayoi, Bunkyo-ku, Tokyo, 113-0032, Japan*

Abstract

We investigate the crustal and upper mantle structure of the Aysén region of Chile from 44° to 49° S, a place where the diverging oceanic Nazca and Antarctic plates subduct beneath the South American continent. The Seismic Experiment in the Aysén Region of Chile (SEARCH) project operated a network of up to 60 land-based seismometers in this region between 2004 and 2006, centered over a 6 Myr old subducted spreading center. The data are used to examine the P wave velocity structure beneath the region using relative-arrival teleseismic travel time tomography, using 2534 P wave residuals from 173 teleseismic earthquakes. It is possible to image the velocity structure beneath the seismic network from ∼30 down to ∼300 km depth. The model can resolve structures at a spatial scale between ∼60 and ∼200 km and shows a large difference between the northern and southern parts of the region. To the north, a ∼100 km thick fast anomaly exists which dips away from the subduction trench; likely to be related to the subducting Nazca plate. Going to the south, as the age of this plate at the subduction trench decreases and arc volcanism shuts off, the fast anomaly migrates further from the trench, suggesting that the Nazca plate subducts at a reduced angle over a larger distance before the subduction angle steepens. The distinct sections of the fast anomaly suggest that slab tears exist across the fracture zones between subducted plate segments. Where the 6 Myr old subducted ridge segment is predicted to lie, there is a region of low velocity between ∼100 and ∼300 km depth, and no fast region associated with a subducting slab is present, indicating the presence of an asthenospheric window between the subducted Nazca and Antarctic plates.

Keywords: Chile Triple Junction, Seismic Tomography, Slab Window, Slab Tear

1. Introduction

The western South American margin, comprising the Nazca and Antarctic oceanic plates and the South American continent, is an outstanding example of a large scale ocean-continent collision zone. While the northern and central parts of this subduction zone have been intensively studied, less is known about the southern extent, in part due to its difficult accessibility. The Nazca plate subduction, which begins at the Chile Triple Junction (CTJ) at ∼46°S and ends at the Cocos-Nazca spreading center at ∼3°N, has a N-S oriented trench in the south. The age of the subducting Nazca plate ranges from 0 Ma at the CTJ to a maximum of ∼60 Ma at around 20°S. The age of the subducting Antarctic plate increases to the south, from 0 Ma at the CTJ to 24 Ma at the southern limit of the continent (Herron et al., 1981; Cande and Leslie, 1986; Seton et al., 2020).

Figure 1 shows the oceanic spreading centers and transform faults between the Nazca and Antarctic plates meeting the subduction trench at the CTJ at ∼46°S. The southern part of the Nazca plate subduction displayed here exhibits strong seismic and tsunamogenic potential (Cisternas et al., 2005), as shown by the 1960 Valdivia earthquake which had a ∼1200 km long rupture from 37°S to approximately the position of the CTJ (Barrientos and Ward, 1990; Moreno et al., 2009) which acts as a natural physical barrier to rupture propagation (Cifuentes, 1989; Tassara, 2010). While the geometry of the subducting oceanic plate is well constrained by deep seismicity to the north, this deep seismicity is lost at ∼42°S (Wortel and Vlaar, 1978; Ruiz and Madariaga, 2018). The arc volcanism, running parallel to the Chilean trench subduction, has two distinct volcanic gaps between the Central, Southern and Austral volcanic zones (Notsu et al., 1987; Futa and Stern, 1988; Ramos and Kay, 1992); one where there is the Pampean flat-slab segment below central Chile and Argentina associated with the subduction of the Juan Fernandez ridge (27-33°S); the other running south from the CTJ, from 46 to 49°S (Stern, 2004). This latter volcanic gap has been attributed to the dehydration of the oceanic slab in the subduction complex at shallow depths (Mpodozis et al., 1985), possible flat-slab subduction shutting off arc magmatism (Suárez et al., 2000), and the limits being at the border of a slab window (Gutiérrez et al., 2005; Groome and Thorkelson, 2009; Georgieva et al., 2019).

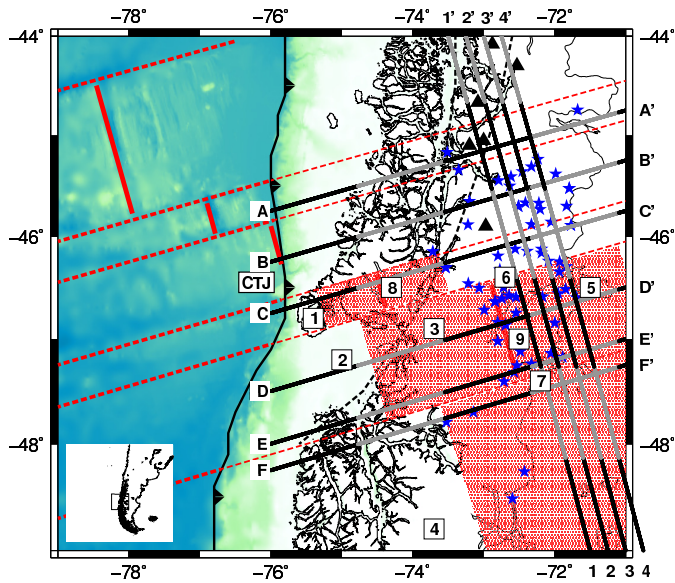*Corresponding Author: mrmiller@udec.cl

Figure 1: Tectonic setting in the region of the Chile Triple Junction, known as the Aysén region of Chile, showing the approximate positions of the spreading centers (red lines), the approximate maximum sizes of the slab windows for the 3, 6 and 10 Ma subducted ridges (red stippled area), fracture zones (dashed red lines), subduction trench (black barbed line), the Liquiñe-Ofqui fault system (dashed black lines), volcanic centers (black triangles) and the seismic stations used in this study (blue stars). The volcanic centers (those with activity within the last 10,000 years) are taken from Siebert and Simkin (2002). The profiles used to display the tomography are represented by the lines A-A' to F-F' for cross sections parallel to the fracture zones, and 1-1' to 4-4' for cross sections perpendicular to the fracture zones; the lines representing these profiles alternate colour between black and gray every 100 km. Places of interest in the region are labelled 1-9. 1 - Taitao Peninsula; 2 - Golfo de Penas; 3 - northern ice field; 4 - southern ice field; 5 - Lago General Carrera / Buenos Aires; 6 - Murta basalts; 7 - Meseta del Lago Buenos Aires basalts; 8 - the 3 Ma subducted ridge; 9 - the 6 Ma subducted ridge. The inset shows the location of the study region within South America.

Oblique subduction of the spreading ridge system beneath the South American plate began 14-15 Ma when a segment of the ridge collided with the subduction trench at ~55°S, generating the CTJ. Since then the triple junction has migrated northwards (although when transform faults are being subducted, the triple junction actually migrates south (Cande et al., 1987)), and ridge segments have been subducted between 14 and 10 Ma , at 6 Ma, and at 3 Ma. The triple junction is currently in a ridge-trench-trench configuration; the ridge segment currently at the triple junction began subducting ~0.3 Ma (Cande and Leslie, 1986). The Taitao Peninsula, approximately 40 km SE of the CTJ, is commonly linked to the subduction of the Chile ridge system, shows a shallow low velocity zone, located beneath hot springs (Gallego et al., 2010), and contains geological units of enriched mid-ocean ridge basalts and ophiolite (Lagabrielle et al., 1994; Veloso et al., 2005, 2007).

North of the CTJ, the Nazca plate is currently subducting at an estimated 75 mm/yr in the direction N77E while to the south the Antarctic plate is currently subducting at 16 mm/yr in an N100E direction (Breitsprecher and Thorkelson, 2009). In the region of the CTJ, known as the Aysén region of Chile,

the South Chile Ridge consists of short spreading centers separated by a series of parallel fracture zones. Therefore the age of the sea floor at the trench changes over the same length scale, from 0 Myr at the spreading center which is currently subducting, to ~2 Myr when crossing the first fracture zone to the north, to ~5 Myr when crossing the second fracture zone further northwards. The approximate locations of the subducted spreading centers, displayed in Figure 1, were directly calculated from the positions of the magnetic anomalies observed by Cande and Leslie (1986) and broadly agree with later studies (Breitsprecher and Thorkelson, 2009; Eagles et al., 2009; Lagabrielle et al., 2015). The extent of the slab windows in Figure 1 assumes that the spreading rate does not diminish after ridge subduction. The two subducted spreading centers in the study region have ages of ~3 Myr and ~6 Myr.

The subduction of active oceanic spreading centers below continental plates is thought to produce a slab window, in this case where the tail end of the Nazca plate is subducting at a faster rate than the front end of the Antarctic plate, and a gap appears between the two subducting plates (Lagabrielle et al., 2000; Daniel et al., 2001), allowing decompression melting of upwelling asthenosphere from sub-slab regions (Thorkelsen, 1996). Magmas generated under these conditions are thought to reproduce the chemistry of the asthenospheric mantle beneath the subducting plate although they may suffer contamination from the crust (Gorring et al., 1997; Thorkelson and Breitsprecher, 2005). Evidence for the presence of slab windows comes from analysis of Quaternary basalts near Murta, at 46.5°S, 72.7°W (Demant et al., 1998; Corgne et al., 2001; Lagabrielle et al., 2004), and isotopic geochemical analysis of flood basalts from the Meseta del Lago Buenos Aires, approximately 100 km further east (Ramos and Kay, 1992; Gorring et al., 2003; Espinoza et al., 2005).

Teleseismic tomography carried out by Russo et al. (2010) shows the presence of the slab window as an anomalously slow region to the south-east of the CTJ from 100 to 200 km depth, and high-velocity anomalies further north associated with the Nazca subduction zone. Strong, predominantly E-W, shear wave splitting is observed in the region, interpreted as asthenospheric flow into and within the slab window coincident with an absence of mantle lithosphere (Russo et al., 2010; Ben-Mansour et al., 2022). This window is also characterized by a large negative Bouguer anomaly of about -60 mGal (Murdie et al., 2000), crustal thinning (Rodriguez and Russo, 2019) and high heat flow (Avila and Dávila, 2018). Mark et al. (2022) produce an extended tomographic image across the entirety of the Patagonian slab window, observing low seismic velocities within the window and evidence for thermal erosion of the lithospheric mantle for the younger slab windows. Guivel et al. (2006) use geochronometric and geochemical evidence for slab tearing between adjacent subducting slab segments, prior to ridge subduction, through which subslab asthenospheric mantle can rise to eventually manifest as plateau basalts. The slab tearing model has also been proposed to explain the chemical signature of volcanism in Mexico (Pallares et al., 2007). The

plateau basalts in the region of the CTJ are observed both pre- and post-ridge subduction (for example, Kay et al. (1993); Espinoza et al. (2008)), and therefore are associated with processes both before and after the ridge subduction.

The subduction of an active spreading centre and young warm oceanic crust can have a major thermal impact on the overlying arc crust, the overlying mantle wedge, and the subducted oceanic crust. The subduction of an active spreading ridge can cause extensive magmatism and both low- and high-P/T metamorphism, generating a significant amount of continental crust growth through arc magmatism (Iwamori, 2000) and explaining the observed characteristics of paired metamorphic belts, such as the Ryoke and Sanbagwa belts in Japan (Iwamori and Zhao, 2000). Recorded heat flow values in the vicinity of the CTJ reveal localized high heat flow and peaks associated with normal faulting within the accretionary prism, potentially corresponding to pathways of hot fluid ascent (Villar-Muñoz et al., 2021). Nonvolcanic tremors have been observed in the vicinity of the CTJ, promoting the existence of a shallow region capable of brittle-ductile behavior and slip on planes characterized by high pore fluid pressures (Ide, 2012; Gallego et al., 2013; Sáez et al., 2019).

The N-S trending Liquiñe-Ofqui fault zone, shown in Figure 1, is one of the most striking features in this area. This fault is a transpressional right-lateral shear zone which bounds the eastern margin of an elongated forearc sliver, the Chiloé block (Cembrano et al., 2000). Oblique convergence of the Nazca plate can cause the Chiloé block to move northward away from an extensional zone located in the CTJ area (Forsythe and Nelson, 1985; Murdie et al., 1993; Cembrano et al., 2002); these models corroborate with GPS measurements (Wang et al., 2007) and anisotropy studies (Murdie and Russo, 1999; Russo et al., 2010; Gallego et al., 2011). The Golfo de Penas (located in Figure 1) is then interpreted as a pull-apart basin. Two regions of elevated topography exist in this region, the northern and southern ice fields. The northern ice field is bounded to the north by the landward projection of the CTJ and is located 50 km westward of the current position of the 6 Myr subducted ridge. These granitic mountains are of Miocene age, and during their uplift they have been unroofed by the erosion of 4-5 km of overlying rocks. The southern ice field has slightly lower elevation but still shows high topography 14-10 Myr after the ridge collision at these latitudes (Folguera and Ramos, 2002; Ramos, 2005). Rapid glacial isostatic rebound indicates low viscosities in the slab window region (Mark et al., 2022).

Sparse, low magnitude, crustal seismicity has been observed in the field area, the majority attributed to the Liquiñe-Ofqui fault system and Hudson Volcano (Agurto-Detzel et al., 2014). The lack of subduction inter-plate seismicity in the area limits the effectiveness of a local tomography in this region, and therefore current existing models use alternative techniques. Gallego et al. (2010), through ambient seismic noise tomography, find low velocities correlating with the volcanic arc of the Southern Volcanic Zone and also the subducted Chile Ridge in the

Taitao Peninsula. Russo et al. (2010), through teleseismic tomography, show direct evidence for the long-hypothesized slab window as a distinctly slow region to the south of the CTJ landwards projection; further north, the subducted Nazca slab is visible as a fast anomaly. This study follows a similar tomographic technique to Russo et al. (2010), using a different dataset that enhances some features of this subduction setting.

2. Data and Methods

2.1. Data

The Seismic Experiment in the Aysén Region of Chile (SEARCH) project was a passive seismic network located from 44.7° to 48.6°S in southern Chile (IRIS network code: XJ). The network comprised sixty broadband seismometers: fourteen CMG-3T sensors and six CMG-40T sensors deployed in January 2004, and forty CMG-6TD sensors deployed in January 2005. All instruments were retrieved in February 2006, resulting in a deployment period of between twelve and twenty four months at each site, during which numerous teleseismic arrivals were recorded. All stations were installed with the aim of coupling the sensor directly to bedrock, far from anthropogenic and environmental noise sources. The relatively low noise levels of the broadband instruments permitted many teleseismic *P* waves to be observed with coherent waveforms between the stations over several cycles, which form the basis of the data set.
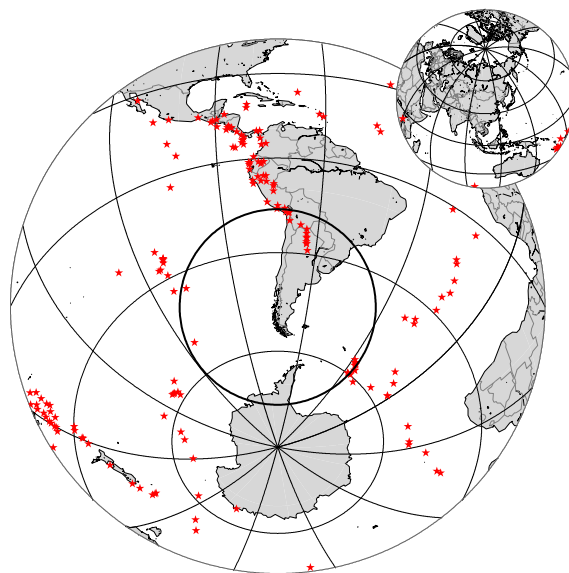

Figure 2: Distribution of the 173 events used in the *P* inversion (red stars). The events further than 90° away are displayed on the inset hemisphere. The small circle indicates a distance of 30° from the seismic array. The events closest to the array to the north have depths of over 500 km.

All teleseismic earthquakes of magnitude 5.0 or greater with a single *P* wave arrival (according to the IASP91 Earth model

(Kennett and Engdahl, 1991)) were inspected visually to determine if the arrival was clearly observed above the noise levels at several stations of the network. The basis of this tomography is that the waveforms should only show minor differences between stations, and based on the visual inspection an initial quality rating [1-3] was assigned to each event. Initially, 280 events were identified that were suitable for this study; however, in areas with high earthquake density (Tonga Trench, Central America, South Sandwich Islands, Southern Peru and Ecuador) we later removed the lower quality events from the data set as their inclusion would not have improved the model. Ultimately, a subset of 173 teleseisms were used whose geographical distribution is shown in Figure 2.

2.2. Measurement of Traveltime Residuals

The data preparation traveltime residual analysis are done on data in the Seismic Analysis Code (SAC) format (Goldstein et al., 2003) using the Multi-Channel Cross Correlation (MCCC) method of VanDecar and Crosson (1990). The instrument response was removed from the seismograms, the mean and linear trend removed and a Hanning taper applied. The seismograms were bandpass filtered between 0.4 and 2 Hz, and a window was chosen between 0.2 s before to 2.2 s after the manual P pick. The selected filter and window ranges improve the waveform correlation between the stations, by increasing the signal:noise ratio and ensuring that several periods of the P phase were included in the calculation. With these chosen values, correlation values remain high even for station pairs separated by several hundreds of kilometers (see Figure S1 in Section S1). The MCCC method cross-correlates the seismograms in this time window producing a set of delays between station pairs, as given by the maxima of the cross-correlation function. Due to noise in the seismograms, the relative arrival times between different station pairs are not perfectly consistent (i.e. $\Delta t_{12} + \Delta t_{23} \neq \Delta t_{13}$, where Δt_{ij} is defined as the MCCC-derived relative delay time between the ith and jth traces). Therefore the optimum relative arrival times are made by minimizing the total error in the system of equations

$$t_i - t_j = \Delta t_{ij} \quad i = 1, 2, ..., n-1; j = i+1, i+2, ..., n \quad (1)$$

for n stations, where t_i represents the optimized arrival time for the ith station, relative to a constrained zero mean. Example correlations resulting from this procedure are displayed in Figure 3 for the three quality ratings.

The MCCC method estimates the uncertainty associated with each relative arrival time by calculating the standard deviation of the residuals associated with the arrival at that particular station (given by Equation 1, for a certain i). A small number of individual traces with standard deviations > 0.2 s were visually inspected and removed at this stage to reduce the possibility of cycle skipping, and the correlation program rerun without these traces to realign the remaining waveforms. The error estimates for MCCC however are usually too optimistic (Tilmann et al., 2001) and it was considered better to estimate error in the picking procedure by comparing the relative arrival

times between station pairs for two teleseisms whose hypocenters are separated by less than 1° and therefore sample the same near-receiver structure. Using the original data set of 280 events, to provide a large number of similarly-positioned teleseisms, the picking error was found to be 0.085 s. For quality 1, 2 and 3 events, respectively, this error is 0.03, 0.08 and 0.13 s.
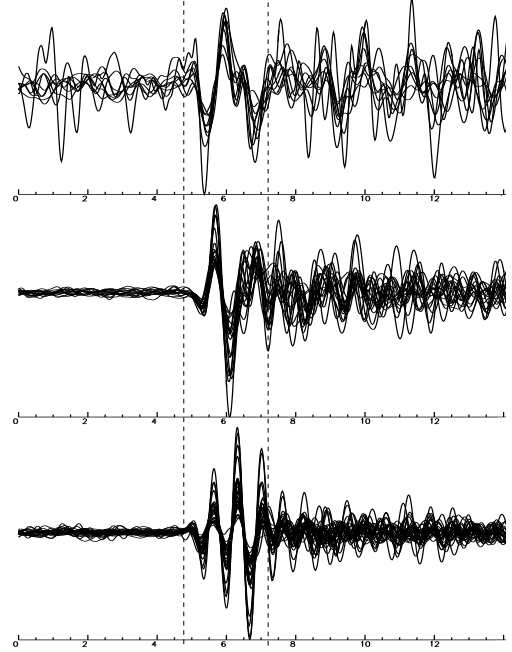

Figure 3: Seismic stacks showing three different P arrivals, centered around the arrival times calculated by MCCC within the 2.4 s time window indicated by the dotted vertical lines. Top: Event origin time 2005-048-01:19:16.5, assigned a quality rating 3. Middle: Event origin time 2005-218-07:36:29.4, assigned a quality rating 2. Bottom: Event origin time 2005-091-07:36:58.3, assigned a quality rating 1.

2.3. Tomographic Inversion Scheme

The inversion method used here is from Bostock and VanDecar (1995) with additional information contained in VanDecar (1991). Traveltime variations can be used to estimate the velocity structure in the vicinity of the network by assigning them as perturbations in the P wave slowness relative to the IASP91 model (Kennett and Engdahl, 1991). The use of relative traveltimes, constrained by zero mean, implies that all perturbations are relative rather than absolute. It is assumed that model perturbations are sufficiently small for the ray paths through the model to be approximated by those through the unperturbed one-dimensional structure. This reduces the initially non-linear inversion to a linear one, in which the traveltime perturbation for the ith ray can be discretely expressed using nodes as

$$\Delta t_i = \sum_j P_{ij} \Delta s_j \quad (2)$$

where j identifies the jth slowness parameter and P_{ij} is the Fréchet derivative $\partial t_i / \partial s_j$ of the ith ray at the jth node. Here,

4

the slowness is defined at certain nodes in the region of interest and is interpolated between them using splines under tension (Cline, 1981).

Additionally, the observed residual traveltimes can be influenced by other factors: the near-surface structure underneath the stations, the spatial uncertainty in the hypocenters of the events used, and the station elevations. As the teleseismic rays have low incidence angles, there is no crossing of rays directly beneath stations to a depth of approximately 30 km for the network used. A traveltime correction, Δt_c, can be applied dependent on ray incidence angle α and a static term c unique to each station:

$$\Delta t_c = c / \cos \alpha \tag{3}$$

To account for spatial uncertainties in hypocentral location, an event-specific correction time Δt_h is also incorporated into the inversion (discussed in the Supplmentary Material Section S3), and finally a station elevation correction Δt_e was applied to account for differences between station elevations. The near-surface P wave velocity for the station correction term was estimated to be 4.8 kms^{-1}; any error in this value is incorporated into the traveltime correction Δt_c and does not change the final tomographic image.

Therefore the traveltime anomaly of the ith ray is

$$\Delta t_i = \Delta t_c + \Delta t_h + \Delta t_e + \sum_j P_{ij} \Delta s_j \tag{4}$$

This equation is solved simultaneously for all rays using the iterative method of conjugate gradients (Scales, 1987). To minimize the effects of outliers on the solution, residuals that fall more than 1.5 standard deviations from the mean are iteratively downweighted (Huber, 1981). In line with, Tilmann et al. (2001), 1000 conjugate gradient iterations and 5 Huber iterations for downweighting outliers were used.

In order to apply the tomographic inversion scheme, the slowness model is represented by a grid of 63,945 nodes beneath the seismic network, extending to 400 km depth. The smallest grid spacing in the resolved area underneath the network is approximately 10 km, smaller than the resolution limit of this study. The precise node positions are detailed in Section S2. Equation (4) was solved for all rays simultaneously subject to smoothing and flattening constraints, on the first and second derivatives of the velocity model, and damping of the spatial hypocenter relocations and station terms. Various damping parameters were tested in the inversion with historically-acceptable values for the hypocenter damping, station damping and the ratio between flattening and smoothing parameters from Tilmann et al. (2001) ultimately used in the inversion. The optimal value for the flattening parameter is data- and network-dependent; this value was determined by minimizing the residuals of a subset of half the traveltime data in a velocity model generated by the inversion of the other half. For flattening parameters lower than this the output starts to show small-scale

spatial velocity variations which fit the noise in the data. A full description of this process can be found in Section S3. The final damping parameters used in the inversion are displayed in Table 1.

Damping Parameter	Value
Model Flattening	0.5 km^{2}s^{-1}
Model Smoothing	10 km^{3}s^{-1}
Station Terms	10 s^{-1}
Hypocenter Perturbations	0.0025 km^{-1}

Table 1: The damping parameters used in the tomographic inversion.

3. Results

3.1. Model Resolution

The range of frequencies used in this study, and the minimum distance between stations in the network, provide a theoretical best resolution of approximately 10 km. However, the ray path distribution is the limiting factor in this study. Therefore, the resolution of the tomographic model is investigated through the recovery of synthetic traveltime data generated by test velocity models. Alternating blocks of 5% fast- and slow-velocity regions, separated by regions of zero velocity perturbation provide the input checkerboard. Several models were produced with differently sized blocks to assess the spatial range of resolvable structures, smaller length scales being resolved do not necessarily guarantee the same about larger structures (Lévêque et al., 1993). Noise was added to the synthetic data from a Gaussian normal distribution with a standard deviation the same as the data error for the different quality events (see Section 2.2), ensuring a representative synthetic data set. The output checkerboard model is subsequently produced using the optimal inversion parameters.

The checkerboard tests, presented in Figures 4 and S4, show that the resolution is acceptable for a range of block sizes from 0.5° x 0.5° x 60 km to 2° x 2° x 200 km. The resolution is best underneath the network, away from this region there are fewer crossing rays and the anomaly size subsequently becomes less defined and smeared along the ray directions. As the block size decreases, this smearing becomes more apparent. For the block size 0.75° x 0.75° x 90 km the recovery of the anomalies extends to around 300 km depth underneath the network and the individual blocks are well resolved, with little smearing. While the distribution of the anomalies is accurately represented, especially beneath the network, their magnitude is slightly underestimated.

In the final models, areas with ray path density of less than 0.01 km^{-2} are shown with reduced brightness, and are shown in gray when the ray path density drops below 0.001 km^{-2}. These values were chosen based on the resolution tests to indicate areas which are at the limit of resolution to areas not
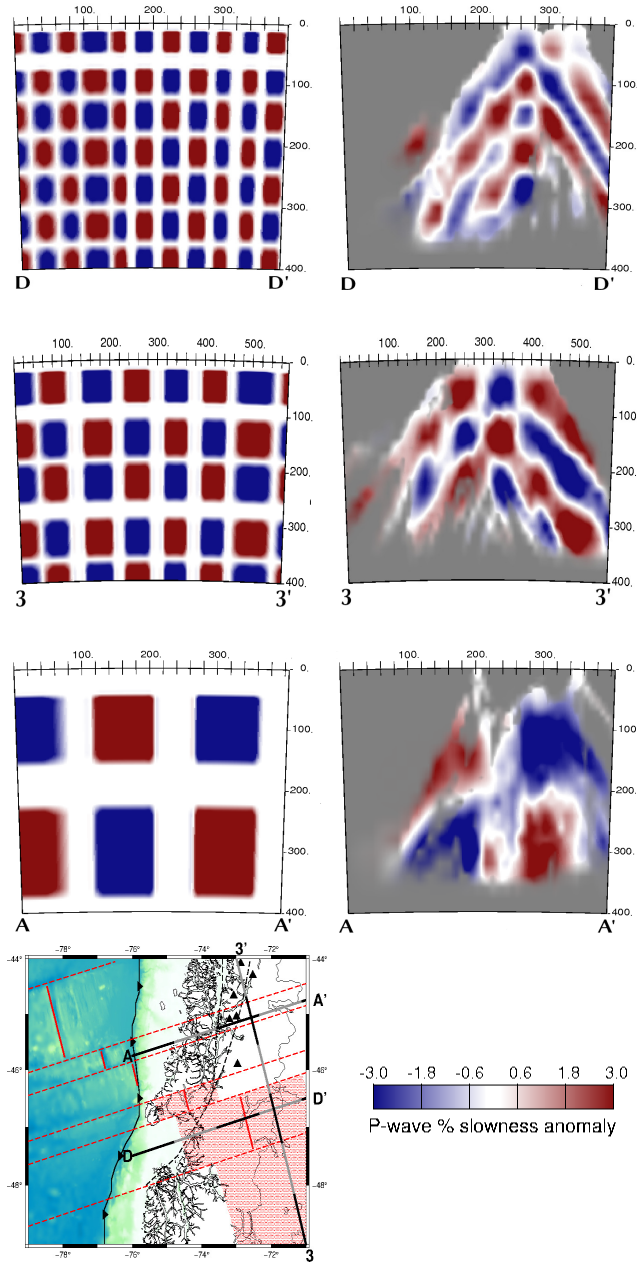
3.2. Station Correction Terms

Figure 5 shows the station correction terms, Δt_c, obtained from the tomography inversion. These corrections are likely due to crustal or upper mantle velocity anomalies which are spatially large enough to affect rays from all backazimuths. The depth extent of these anomalies is roughly the station spacing, so is as low as 20 km in the centre of the network but up to ~60 km for peripheral stations. A negative station correction term corresponds to fast shallow anomalies; a positive station correction term the opposite. It should be noted that the station correction terms can absorb mantle structure even below the crossing depth (Priestley and Tilmann, 2009); however, the tomographic features discussed in this study are robust enough to appear on the images produced by inversions both with and without station correction terms included. The station correction terms reduce the standard deviation of the traveltime residuals from 0.33 to 0.27 s. This standard deviation is then further reduced to 0.08 s by the tomographic inversion, similar to the estimated picking error of the dataset calculated in Section 2.2.
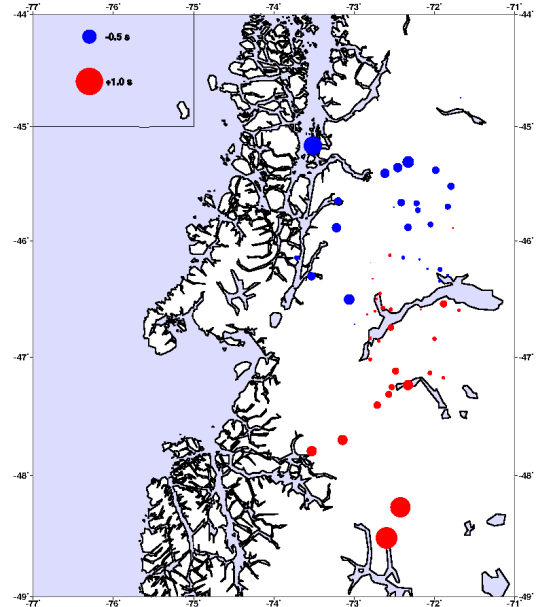
Figure 4: Checkerboard resolution tests for selected cross sections and block sizes: horizontal distance is along the profile in km, vertical distance is depth in km. The specific cross sections are displayed in the map, alternating color between black and gray every 100 km, the geological features of the map are the same as in Figure 1. The slowness anomaly is presented as a percentage deviation from the reference IASP91 velocity model. Areas of low ray coverage, less than 0.01 km^{-2}, are shown with reduced brightness at the edge of the illuminated region and areas with ray coverage lower than 0.001 km^{-2} are covered in gray. Of each pair, on the left are the original synthetic slowness models and on the right are the reproduced models by the inversion. Top: resolution test for block size 0.5° x 0.5° x 60 km for profile D-D'. Middle: resolution test for block size 0.75° x 0.75° x 90 km for profile 3-3'. Bottom: resolution test for block size 2° x 2° x 200 km for profile A-A'. Additional checkerboard tests are shown in the Supplementary Material Section S4.

Figure 5: The station correction terms, Δt_c, for the stations used in the tomography study. The blue circles indicate stations where arrivals are earlier than expected, with red circles indicating stations where the arrivals are later than expected. The size of the circle gives the magnitude of the correction, with the scale shown in the top left corner.

3.3. Tomographic Model

The tomographic model resulting from the traveltime inversion is shown in Figures 6, 7 and 8. The fast and slow anomalies that exist in the mantle are up to ~3%, although the maximum values may be slightly underestimated due to smearing. To investigate the distribution of these anomalies we consider cross sections, both parallel and perpendicular to the offshore fracture zones. Figure 1 shows the cross sections; those parallel to the fracture zones show the subduction settings where oceanic lithosphere of different ages are at the trench:

resolved. Furthermore, as shown by the resolution tests, smearing of anomalies not directly underneath the network should be taken into account when interpreting the results.
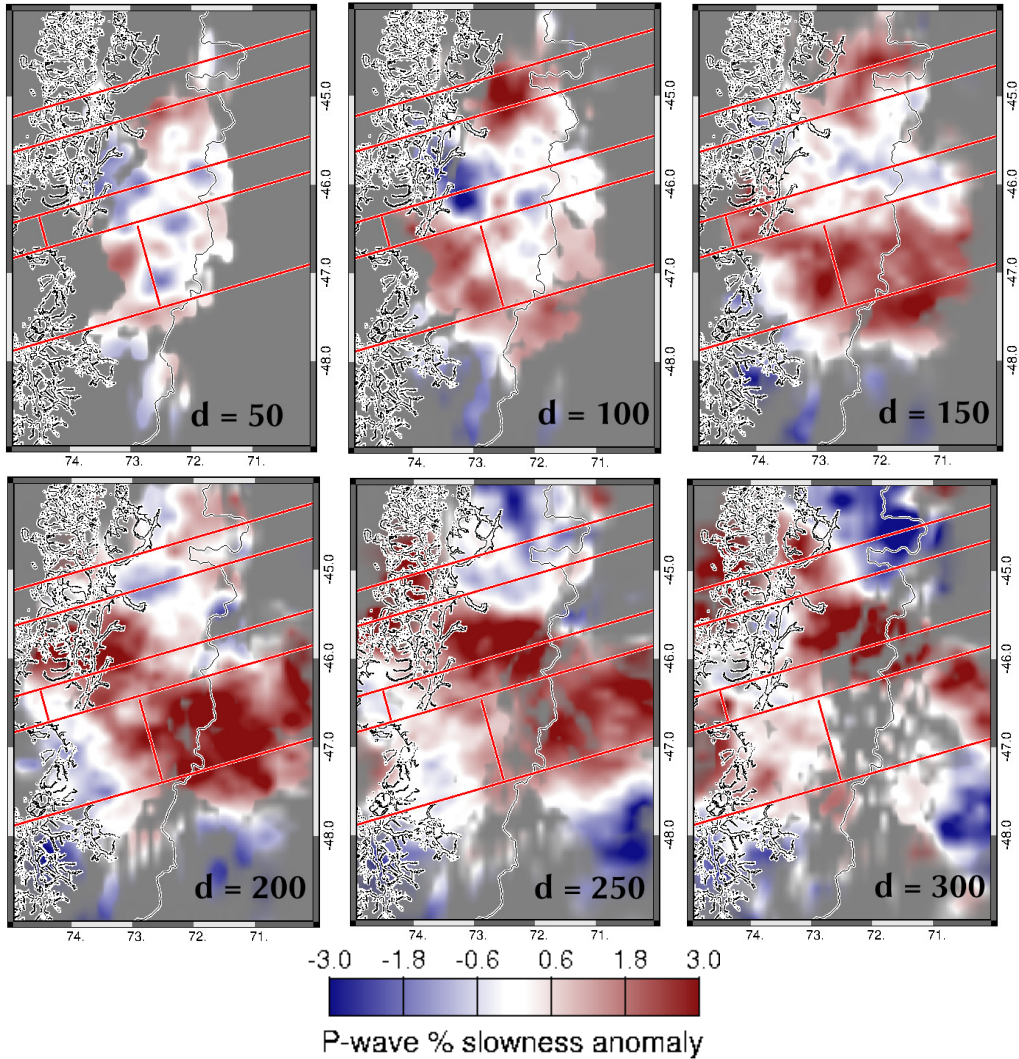
Figure 6: The tomography results for depth slices of the model at depths of 50, 100, 150, 200, 250 and 300 km. The coastline and Chile-Argentina border are included for reference, the ridge and transform system indicated by the red lines is the same as that displayed in Figure 1. The slowness scale is presented as a percentage deviation from the reference IASP91 velocity model. Areas of low ray coverage, less than 0.01 km^{-2}, are shown with reduced brightness at the edge of the illuminated region and areas with ray coverage lower than 0.001 km^{-2} are covered in gray.

From profile A-A' in the north (where ~2 Myr old Nazca plate is currently being subducted (Lagabrielle et al., 2004)) to profile F-F' further south (where ~6 Myr old Antarctic plate is currently being subducted). The profiles 1-1' to 4-4' running perpendicular to the fracture zones cross the different subduction settings encountered in the region.

The final tomographic model is, to first order, largely similar, in both the amplitude and distribution of the velocity perturbations, to Russo et al. (2010). The northernmost part of the region contains, in general, higher Vp anomalies, for example see the ~300 km deep fast anomaly at 45°S, 72°W in Figure 6. At latitudes below the CTJ a large low Vp anomaly resides in the estimated slab window position between 100 and 300 km depth, for example see the ~200 km deep slow anomaly centered around 47°S, 72°W in Figure 6. These general features are similarly interpreted to be the subducted Nazca plate in the

north of the field area, and the slab window south of the CTJ, formed by the continued separation of the Nazca and Antarctic plates. The resolution tests run in this study indicate however that smaller-scale structures can be resolved beneath the network, especially in the north of the study area which has greater ray coverage and density. The following discussion considers in greater detail the features displayed in the tomography.

4. Discussion

The station correction terms (Figure 5) have an amplitude of less than 0.5 seconds below the centre of the network and increase to just under 1.0 seconds for the peripheral stations; they show a clear pattern: negative in the northern part of the network and positive in the southern, with the change between negative and positive occurring around the latitude of the CTJ. While these terms can not indicate the precise depth of the
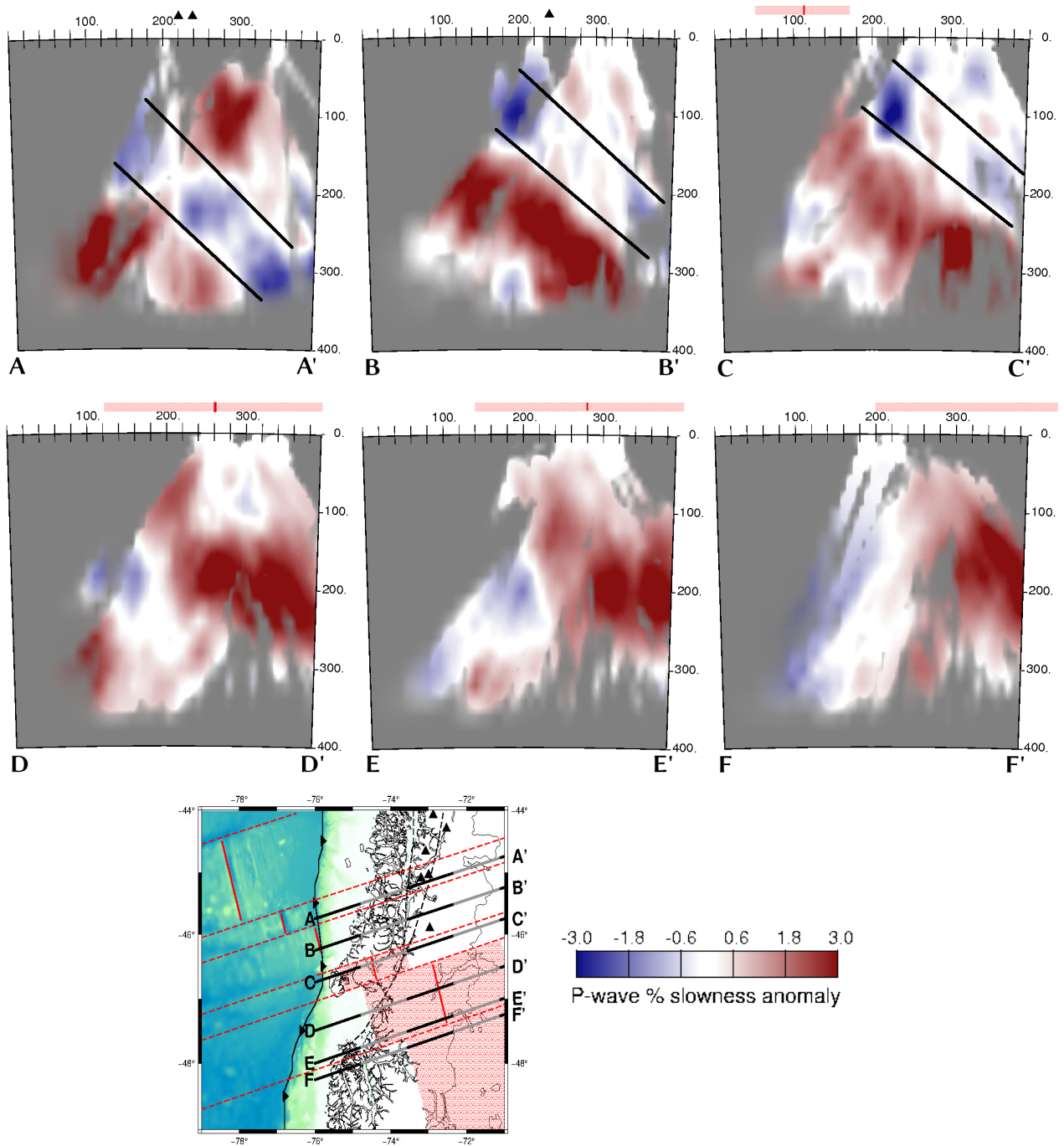
7

Figure 7: The tomography results for the profiles A-A' to F-F' displayed in Figure 1, which run parallel to the fracture zones of the ridge system which is being subducted, distance units are in km. The specific cross sections are displayed in the map, alternating color between black and gray every 100 km, the geological features of the map are the same as in Figure 1. The slowness scale is presented as a percentage deviation from the reference IASP91 velocity model. Volcanic centers within the subduction profiles A-A' and B-B' are shown as black triangles above the horizontal scale. The proposed approximate upper and lower limits of the subducting slab are shown in the subduction profiles A-A' to C-C'. The maximum slab window sizes for the subduction profiles C-C' to F-F' are shown as a red stippled area above the horizontal scale, with the approximate ridge location the red vertical line. Areas of low ray coverage, less than 0.01 km^{-2}, are shown with reduced brightness at the edge of the illuminated region and areas with ray coverage lower than 0.001 km^{-2} are covered in gray.

shallow anomalies that produce them, their general N-S trend agrees well with receiver function crustal thickness measurements (Rodriguez and Russo, 2019), increased heat flow (Avila and Dávila, 2018) and the hypothesis of thermal erosion of the lithospheric mantle for the younger slab windows (Mark et al., 2022).

Profile A-A', in Figure 7, displays a cross section where the Nazca plate has an age of ~2 Myr at the subduction trench. In this profile a fast anomaly exists, with around 100 km thickness, dipping from the trench to the east. We interpret this anomaly as the subducting Nazca plate, as it has
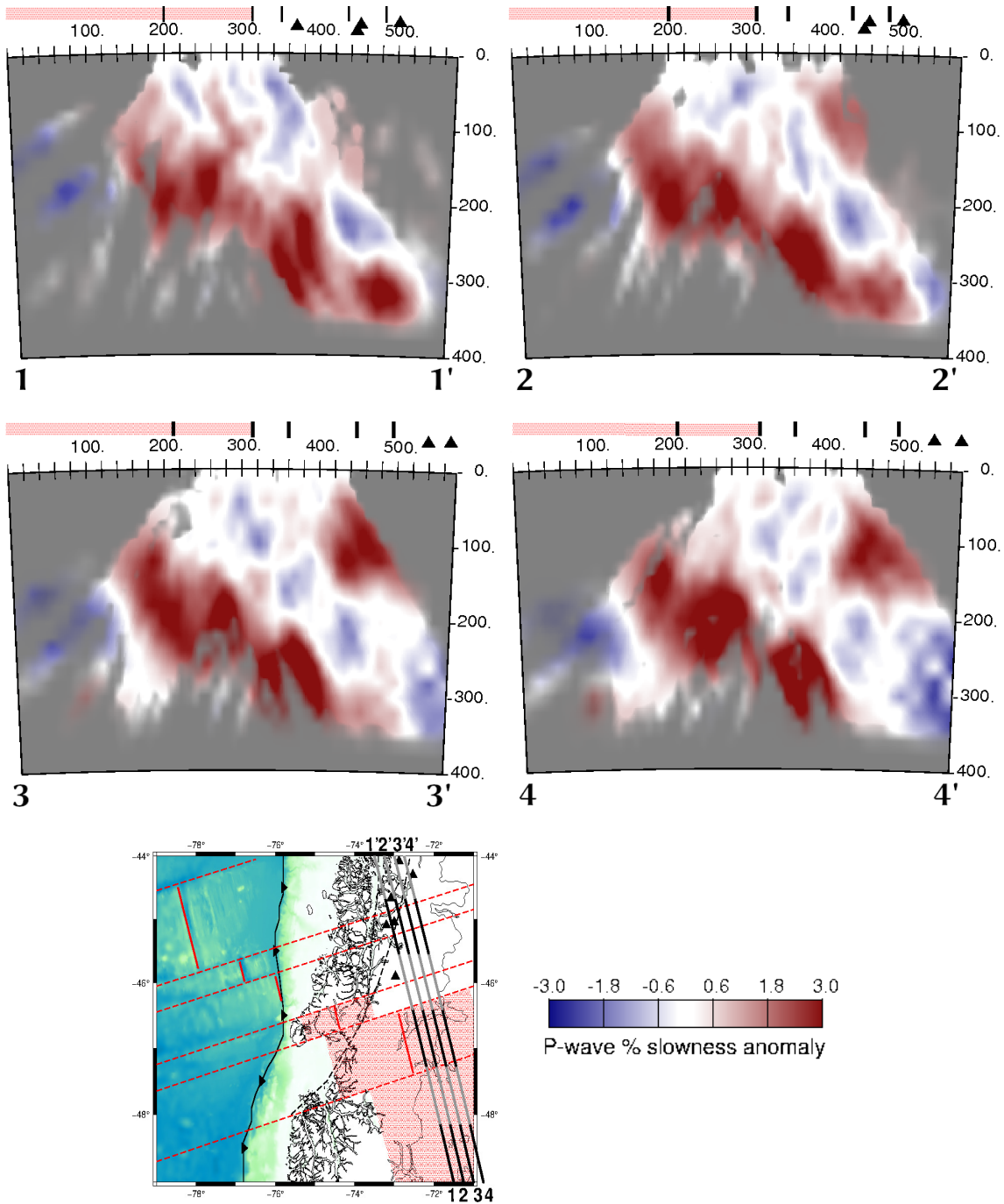
Figure 8: The tomography results for the profiles 1-1' to 4-4' displayed in Figure 1, which run approximately south to north perpendicular to the fracture zones of the ridge system which is being subducted, distance units are in km. The specific cross sections are displayed in the map, alternating color between black and gray every 100 km, the geological features of the map are the same as in Figure 1. The slowness scale is presented as a percentage deviation from the reference IASP91 velocity model. Volcanic centers close to the profiles are shown as black triangles above the horizontal scale. The slab window sizes are shown as a red stippled area above the horizontal scale. The black vertical lines above the horizontal scale show where the profiles cross fracture zones. Areas of low ray coverage, less than 0.01 km^{-2}, are shown with reduced brightness at the edge of the illuminated region and areas with ray coverage lower than 0.001 km^{-2} are covered in gray.

a similar subduction profile to the Nazca plate further north (Gudmundsson and Sambridge, 1998; Hayes et al., 2018). A local seismicity study from latitude ~42°S (Lange et al., 2007), observes approximately an initial subduction angle of ~10° for the first ~100 km, followed by steeper subduction at ~40°, which correlates with the top of the fast velocity anomaly observed on this profile. While our study cannot determine the subduction structure close to the trench, Scherwath et al. (2009) and Maksymowicz et al. (2012) constrain the initial subduction geometry of the Nazca plate at this latitude, whose dip varies from about 4°, at the trench, to 15° 100 km from the trench at an average dip angle of roughly 10°. A further

9

feature to note is the slow velocity zone (seen most clearly ~300 km along profile A-A' at 100 km depth, and annotated as VA (Volcanic Arc) in the conceptual model of Figure 9) which lies underneath the southernmost volcanoes of the Southern Volcanic Zone, a feature seen also in Gallego et al. (2010). This low velocity region is potentially associated with hydration and melting of the upper plate beneath the volcanic arc at these latitudes, and is a common feature of subduction zones (Zhao et al., 1992; González-Vidal et al., 2018).

Profile B-B' displays a cross section where the Nazca plate has an age of ~0 Myr at the subduction trench. Here, the subducting fast region is dipping at approximately the same angle as in the northern profile but it is moved further to the east. This is interpreted as there being a possible extended initial period of low-dip subduction, with steeper angles starting at a greater distance from the subduction trench, possibly coinciding with the age of the subducted Nazca plate reaching 5-6 Myr. The lack of station coverage above the initial part of this subduction profile near the trench means that this hypothesis can not be confirmed by this study, however a physical change in the subduction zone properties at this latitude is expected as this profile corresponds with the northern extent of the Patagonian volcanic gap where arc volcanism terminates (Stern, 2008). While this part of the discussion is speculative and requires further study, abrupt changes in the dip of the subducting plate have been observed in the north of Chile (Contreras-Reyes et al., 2012) so the suggestion is not too outlandish.

Profile C-C' shows a cross section through the 3 Myr old subducted ridge segment. However, the subducted ridge segment lies only 100 km along the profile and is not resolved. The shallow fast region in this profile is interperted as the young Nazca plate, where the proposed change from a shallower to a steeper subduction angle is yet further from the trench, again potentially in a position where the age of the subducted Nazca plate is 5-6 Myr. However, in general, the resolution of individual features in this profile is compromised by the small width of the subducted ridge segment.

Profiles D-D' and E-E' are cross sections through the 6 Myr old subducted ridge segment. There is a pronounced, ~150 km wide, ~3% slow region 350 km along the profile between approximately 100 and 300 km depth in these cross sections. While it is difficult to obtain the depth range of this anomaly more precisely than this due to model resolution and smearing, this is at the location of the 6 Ma old subducted ridge segment, and is in general agreement with Russo et al. (2010) and Mark et al. (2022). This slow velocity anomaly is therefore proposed to be associated with the asthenospheric window. In profile D-D', regions of shallow (less than 150 km) slow velocity exist 200 and 350 km along the profile from the trench, separated by a region of higher velocity. These regions of slow velocity, while at the limit of resolution, could be upwellings associated with the flood basalt volcanism at Murta/Rio Ibanez (Lagabrielle et al., 2004) and Mesata Chile Chico (Espinoza et al., 2005) which are found at the same distances along the profile.

The southernmost profile, F-F', is a cross section through the subducting Antarctic plate. Unfortunately, the resolution of the features in this profile is low. The poorly-resolved, large low velocity region between 100 and 300 km depths, 200 to 400 km along the profile, could potentially be due to the asthenospheric window from the subduction of the ridge segment 10-14 Ma, as seen in Mark et al. (2022).

The roughly west-east profiles A-A' to F-F' are complimented by four north-south profiles (Figure 8) to show the spatial changes of the tomography model in the direction perpendicular to the subduction zone. If, as we propose, the subduction geometry changes depending on the age of the subducting plate, then due to the abrupt changes in the age of the sea floor at the subduction trench from north to south there should be clearly distinct changes in the positions of the subducted segments of the Nazca plate on the profiles which run perpendicular to the fracture zones. The best resolved profile, 3-3', indeed shows distinct regions of ~100 km thick fast anomalies which start off shallow further south (near the centre of the profile) and then get progressively deeper to the north (going to the right of the profile). The depth of the fast anomaly, which we interpret as the subducted oceanic slab, shows abrupt changes which correlate with the discontinuous changes in the age of the sea floor at the trench. The proposed geometry of the subducted Nazca plate in this study requires substantial aseismic vertical shear between the segments underneath the field area, in agreement with the geochemical analyses of Guivel et al. (2006); Pallares et al. (2007).

In the deeper portion of the velocity model, below the proposed limit for the base of the subducted Nazca plate, a low Vp anomaly is observed on profiles A-A' to C-C', potentially dipping to the east. Such structures have been routinely observed in tomographic studies of subduction zones (Portner et al., 2017). While debate is ongoing as to the robustness of such velocity features, proposed explanations include these low velocities resulting from the entrainment of hot asthenosphere beneath the subducting plate (Liu and Zhou, 2015; Hawley et al., 2016). We suggest a similar explanation is reasonable for the anomalies observed in our model, the asthenospheric subslab material having a slow velocity due to its proximity to an oceanic spreading center. From the north-south profiles in Figure 8, the slow anomaly to the south between 100 and 300 km depth, interpreted to be associated with the slab window, is seen to dip to the north and appears at over 200 km depth below the fast Vp sections interpreted to be the subducting plate. This observation lends further weight to the interpretation of slow asthenospheric subslab material being present in this subduction zone, although this hypothesis is admittedly still speculative.

The proposed conceptual interpretation of the subduction of the Nazca plate near the CTJ is displayed in Figure 9. This model contains spatial variations on a similar lengthscale

within the resolvable range (Section 3.1). The fast sections marked "N" increase in depth from south to north and correlate with the changes in the age of the oceanic plate which is currently being subducted, are of the same dimensions as the blocks in the checkerboard test which can be well recovered, especially underneath the network. Therefore, while the precise subduction geometry is still to be determined, especially close to the subduction trench, the reduction in the depth of the subducted slab from north to south underneath the network, as the Nazca plate decreases in age, is resolved in this tomographic study. Such slab tearing between subduction profiles of different ages has been observed in other subduction zones (Millen and Hamburger, 1998; Miller et al., 2006; Dougherty and Clayton, 2014; Meighan et al., 2013) and could explain the chemical properties of the plateau basalts in this region (Guivel et al., 2006) and the presence of magmatism in the region in such places as Murta (Lagabrielle et al., 2004) and Meseta del Lago Buenos Aires (Ramos and Kay, 1992; Gorring et al., 2003; Espinoza et al., 2005); it is worth noting that these places lie on the fracture zones between subduction settings of different age. Vertical slab tearing along subducted fracture zones in this region has previously been hypothesized by Georgieva et al. (2019). Finally, the slab tear to the north of the triple junction proposed by our study would provide a mechanism for plateau basalts to form prior to ridge subduction, as have been observed by Kay et al. (1993) and Espinoza et al. (2008).
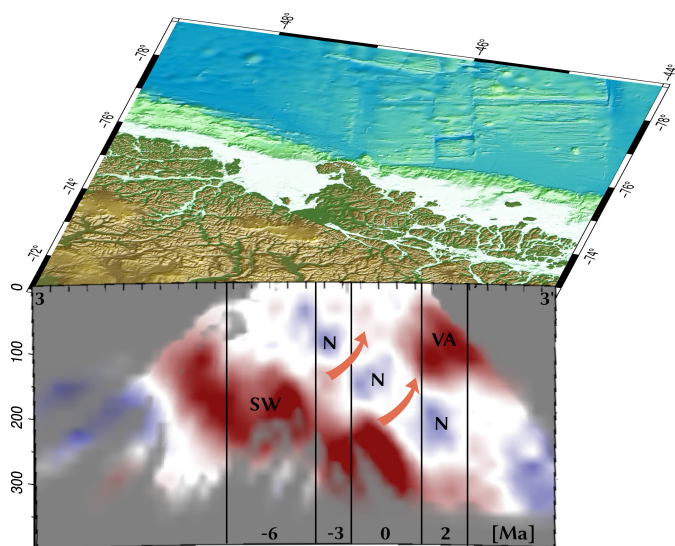

Figure 9: Tomographic profile 3-3', initially presented in Figure 8, aligned over an oblique view of the region. The numbers at the bottom of the profile correspond to the approximate age of the Nazca Plate at the subduction trench, a negative age indicates that the ridge has already subducted that many Myr ago, the vertical lines separate the subduction settings of different ages. SW refers to the Slab Window slow anomaly in the position of the subducted 6 Ma spreading center; VA refers to the slow anomaly below the Volcanic Arc; N refers to the proposed positions of the different subducted segments of the fast anomaly representing the Nazca Plate. The arrows indicate possible pathways for upwelling of mantle material to the north of the Slab Window. A checkerboard resolution test for this profile can be viewed in Figure 4.

5. Conclusions

The tomography model in this study shows the thermal impact of ridge subduction. A ~3% slow *P* velocity anomaly is observed in the region where the 6 Ma spreading centre lies. This anomaly lies generally between 100 and 300 km depths, and extends over a large area, representing an asthenospheric slab window in this region, as seen by Russo et al. (2010).

The tomography images a low velocity region underneath the volcanic arc, which then is not observed in the subsequent profiles south of the end of the Southern Volcanic Zone. Here, the subduction profile has approximately the same geometry as that of the Nazca plate subduction further north (Lange et al., 2007). As the arc volcanism shuts off going further south, the tomographic model appears to show a progressively shallower subducted Nazca plate. The depth of the subducted plate changes discontinuously, following the changes in the plate age at the subduction zone across the fracture zones. Aseismic slab tears along the fracture zones between the successive subduction segments of the Nazca plate near to the triple junction are proposed, which permits a possible explanation for the plateau basalts in Southern Chile and Argentina which formed prior to ridge subduction.

Despite the difficulties introduced by the limited access to various parts of the region, this study begins to answer the questions surrounding the subduction of young oceanic plates and ridge segments. The ultimate aim of projects in this region of Chile will be to determine and explain the tectonic geometry and thermal structure of this unique subduction setting. While there is more work to be done to fully understand this subduction, the results from this study can help to constrain the plate geometry and thermal impact associated with ridge subduction. With the region becoming increasingly accessible, new seismic studies in the region, especially closer to the actual Triple Junction, will increase knowledge about the processes that occur during the Chile Rise subduction.

6. Acknowledgements

images in this study were produced using the software of Wessel et al. (2013). Finally, we enormously appreciate the rapid and thorough revision of this manuscript and the supplementary material by two anonymous reviewers, whose suggestions have made a significant contribution and improvement to these documents.

References

Agurto-Detzel, H., Rietbrock, A., Bataille, K., Miller, M., Iwamori, H., Priestley, K., 2014. Seismicity distribution in the vicinity of the Chile Triple Junction, Aysén Region, southern Chile. J. South Am. Earth Sci. 51, 1–11.

Avila, P., Dávila, F.M., 2018. Heat flow and lithospheric thickness analysis in the Patagonian asthenospheric windows, southern South America. Tectonophysics 747-748, 99–107.

Barrientos, S.E., Ward, S.N., 1990. The 1960 Chile earthquake: inversion for slip distribution from surface deformation. Geophys. J. Int. 103, 589–598.

Ben-Mansour, W., Wiens, D.A., Mark, H.F., Russo, R.M., Richter, A., Marderwald, E., Barrientos, S., 2022. Mantle Flow Pattern Associated With the Patagonian Slab Window Determined From Azimuthal Anisotropy. Geophy. Res. Lett. 49, e2022GL099871.

Bostock, M., VanDecar, J., 1995. Upper mantle structure of the northern Cascadia subduction zone. Canadian Journal of Earth Sciences 32, 1–12.

Breitsprecher, K., Thorkelson, D., 2009. Neogene kinematic history of Nazca-Antarctic-Phoenix slab windows beneath Patagonia and the Antarctic Peninsula. Tectonophysics 464, 10–20.

Cande, S., Leslie, R., 1986. Late Cenozoic tectonics of the southern Chile trench. J. Geophys. Res. 91, 471–496.

Cande, S., Leslie, R., Parra, J., Hodbart, M., 1987. Interaction between the Chile ridge and the Chile trench: Geophysical and geothermal evidences. J. Geophys. Res. 92, 495–520.

Cembrano, J., Liven, A., Reynolds, P., Arancibia, G., Lopez, G., Sanhueza, A., 2002. Late Cenozoic transpressional ductile deformation north of the Nazca-South America-Antarctica triple junction. Tectonophysics 354, 289–314.

Cembrano, J., Schermer, A., Lavenu, A., Sanhueza, A., 2000. Contrasting nature of deformation along an intra-arc shear zone, the Liquine-Ofqui fault zone, southern Chilean Andes. Tectonics 319, 129–149.

Cifuentes, I., 1989. The 1960 Chilean Earthquakes. J. Geophys. Res. 94, 665–680.

Cisternas, M., Atwater, B., Torrejón, F., Sawai, Y., Machuca, G., Lagos, M., Eipert, A., Youlton, C., Salgado, I., Kamataki, T., Shishikura, M., Rajendran, C., Malik, J., Rizal, Y., Husni, M., 2005. Predecessors of the giant 1960 Chile earthquake. Nature 437, 404–407.

Cline, A., 1981. FITPACK - Software package for curve and surface fitting employing splines under tension. University of Texas, Austin, Texas .

Contreras-Reyes, E., Jara, J., Grevemeyer, I., Ruiz, S., Carrizo, D., 2012. Abrupt change in the dip of the subducting plate beneath north Chile. Nature Geosci. 5, 342–345.

Corgne, A., Maury, R., Lagabrielle, Y., Bourgois, J., Suárez, M., Cotten, J., Bellon, H., 2001. La diversité des basaltes de Patagonie á la latitude du point triple du Chili (46-47° lat. S) : données complémentaires et implications sur les conditions de la subduction. Comptes Rendus de l'Académie des Sciences 333, 363–371.

Daniel, A., Kusznir, N., Styles, P., 2001. Thermal and dynamic modelling of deep subduction of a spreading centre: implications for the fate of the subducted Chile Rise, Southern Chile. J. Geophys. Res. 106, 4293–4305.

Demant, A., Belmar, M., Hervé, F., Pankhurst, R., Suárez, M., 1998. Pétrologie et géochimie des basaltes de Murta: une éruption sousglaciaires dans les Andes Patagoniennes (46° lat. S.), Chili. Relation avec la subduction de la ride du Chili. Comptes Rendus de l'Académie des Sciences 327, 795–801.

Dougherty, S.L., Clayton, R.W., 2014. Seismicity and structure in central Mexico: Evidence for a possible slab tear in the South Cocos plate. J. Geophys. Res. 119, 3424–3447.

Eagles, G., Gohl, K., Larter, R., 2009. Animated tectonic reconstruction of the Southern Pacific and alkaline volcanism at its convergent margins since Eocene times. Tectonophysics 464, 21–29.

Espinoza, F., Morata, D., Pelleter, E., Maruy, R., Suárez, M., Lagabrielle, Y., Plové, M., Bellon, H., Cotten, J., 2005. Petrogenesis of the Eocene and Mio-Pliocene alkaline basaltic magmatism in Mesata Chile Chico, southern Patagonia, Chile: Evidence for the participation of two slab windows. Lithos 82, 315–343.

Espinoza, F., Morata, D., Polvé, M., Lagabrielle, Y., Maury, R., Guivel, C., Cotten, J., Bellon, H., Suárez, M., 2008. Bi-modal back-arc alkaline magmatism after ridge subduction: Pliocene felsic rocks from central Patagonia (47°S). Lithos 101, 191–217.

Folguera, A., Ramos, V., 2002. Los efectos producidos por la aproximación, colisión y subducción de dorsales pacíficas en los Andes Patagónicos. Acta Geológica Hispánica 37, 329–353.

Forsythe, R., Nelson, E., 1985. Geological manifestations of ridge collision: Evidence from the Golfo de Penas-Taitao basin, southern Chile. Tectonics 4, 477–495.

Futa, K., Stern, C.R., 1988. Sr and Nd isotopic and trace element compositions of Quaternary volcanic centers of the Southern Andes. Earth Planet. Sci. Lett. 88, 253–262.

Gallego, A., Panning, M., Russo, R., Comte, D., Mocanu, V., VanDecar, J., Murdie, R., 2011. Azimuthal Anisotropy in the Chile Ridge Subduction Region Retrieved from Ambient Noise. Lithosphere 3, 393–400.

Gallego, A., Russo, R., Comte, D., Mocanu, V., VanDecar, J., Murdie, R., 2010. Seismic Noise Tomography in the Chile Ridge Subduction Region, Northern Patagonia. Geophys. J. Int. 182, 1478–1492.

Gallego, A., Russo, R.M., Comte, D., Mocanu, V., Murdie, R.E., VanDecar, J., 2013. Tidal modulation of continuous nonvolcanic seismic tremor in the Chile triple junction region. Geochem. Geophys. Geosyst. 14, 851–863.

Georgieva, V., Gallagher, K., Sobczyk, A., Sobel, E., Schildgen, T., Ehlers, T., Strecker, M., 2019. Effects of slab-window, alkaline volcanism, and glaciation on thermochronometer cooling histories, Patagonian Andes. Earth Planet. Sci. Lett. 511, 164–176.

Goldstein, P., Dodge, D., Firpo, M., 2003. SAC2000: Signal processing and analysis tools for seismologists and engineers. International Handbook of Earthquake & Engineering Seismology Part B, 1613–1614.

González-Vidal, D., Obermann, A., Tassara, A., Bataille, K., Lupi, M., 2018. Crustal model of the Southern Central Andes derived from ambient seismic noise Rayleigh-wave tomography. Tectonics 744, 215–226.

Gorring, M., Kay, S., Zeitler, P., Ramos, V., Rubiolo, D., Fernández, M., Panza, J., 1997. A slab window origin for Neogene Patagonian plateau lavas (46.5° to 49.5°S). Tectonics 16, 1–17.

Gorring, M., Singer, B., Gowers, J., Kay, S., 2003. Plio-Pleistocene basalts from the Meseta del Lago Buenos Aires, Argentina: evidence for asthenosphere-lithosphere interactions during slab window magmatism. Chemical Geology 192, 215–235.

Groome, W.G., Thorkelson, D.J., 2009. The three-dimensional thermomechanical signature of ridge subduction and slab window migration. Tectonophysics 464, 70–83.

Gudmundsson, O., Sambridge, M., 1998. A regionalized upper mantle (RUM) seismic model. J. Geophys. Res. 103, 7121–7136.

Guivel, C., Morata, D., Pelleter, E., Espinoza, F., Maury, R.C., Lagabrielle, Y., Polvé, M., Bellon, H., Cotten, J., M., B., M., S., De la Cruz, R., 2006. Miocene to late Quaternary Patagonian basalts (46-47°S): Geochronometric and geochemical evidence for slab tearing due to active spreading ridge subduction. J. Vol. Geo. Res. 149, 346–370.

Gutiérrez, F., Gioncada, A., González Ferran, O., Lahsen, A., Mazzuoli, R., 2005. The Hudson Volcano and surrounding monogetic centres (Chilean Patagonia): An example of volcanism associated with ridge-trench collision environment. J. Vol. Geo. Res. 145, 207–233.

Hawley, W.B., Allen, R.M., Richards, M.A., 2016. Tomography reveals buoyant asthenosphere accumulating beneath the Juan de Fuca plate. Science 353, 1406–1408.

Hayes, G.P., Moore, G.L., Portner, D.E., Hearne, M., Flamme, H., Furtney, M., Smoczyk, G.M., 2018. Slab2, a comprehensive subduction zone geometry model. Science 362, 58–61.

Herron, E.M., Cande, S., Hall, B., 1981. An active spreading center collides with a subduction zone: a geophysical survey of the Chile Margin triple junction. Geol. Soc. Am. Mem. 154, 683–701.

Huber, P., 1981. Robust Statistics. John Wiley & Sons, New York .

Ide, S., 2012. Variety and spatial heterogeneity of tectonic tremor worldwide. J. Geophys. Res. 117.

Iwamori, H., 2000. Thermal effects of ridge subduction and its implications for the origin of granitic batholith and paired metamorphic belts. Earth Planet. Sci. Lett. 181, 131–144.

Iwamori, H., Zhao, D., 2000. Melting and seismic structure beneath the northeast Japan arc. Geophy. Res. Lett. 27, 425–428.

Kay, S., Ramos, V., Marquez, M., 1993. Evidence in Cerro Pampa volcanic rocks for slab melting prior to ridge-trench collision in southern South America. Geology 101, 703–714.

Kennett, B., Engdahl, E., 1991. Traveltimes for global earthquake location and phase identification. Geophys. J. Int. 105, 429–465.

Lagabrielle, Y., Bourgois, J., Dyment, J., Pelletier, B., 2015. Lower plate deformation at the Chile Triple Junction from the paleomagnetic record (45°30's–46°s). Tectonics 34, 1646–1660.

Lagabrielle, Y., Guivel, C., Maury, R., Bourgois, J., Fourcade, S., Martin, H., 2000. Magmatic–tectonic effects of high thermal regime at the site of active ridge subduction: the Chile Triple Junction model. Tectonophysics 326, 255–268.

Lagabrielle, Y., Le Moigne, J., Maury, R., Cotten, J., Bourgois, J., 1994. Volcanic record of the subduction of an active spreading ridge, Taitao Peninsula (southern Chile). Geology 22, 515–518.

Lagabrielle, Y., Suárez, M., Rossello, E., Hérail, G., Martinod, J., Régner, M., de la Cruz, R., 2004. Neogene to Quaternary tectonic evolution of the Patagonian Andes at the latitude of the Chile Triple Junction. Tectonophysics 385, 211–241.

Lange, D., Rietbrock, A., Haberland, C., Bataille, K., Dahm, D., Tilmann, F., Flüh, E., 2007. Seismicity and geometry of the south Chilean subduction zone (41.5°s - 43.5°s): Implications for controlling parameters. Geophy. Res. Lett. 34, L06311.

Lévêque, J., Rivera, L., Wittlinger, G., 1993. On the use of the checker-board test to assess the resolution of tomographic inversion. Geophys. J. Int. 115, 313–318.

Liu, L., Zhou, Q., 2015. Deep recycling of oceanic asthenosphere material during subduction. Geophy. Res. Lett. 42, 2204–2211.

Maksymowicz, A., Contreras-Reyes, E., Grevemeyer, I., Flueh, E.R., 2012. Structure and geodynamics of the post-collision zone between the Nazca–Antarctic spreading center and South America. Earth Planet. Sci. Lett. 345-348, 27–37.

Mark, H.F., Wiens, D.A., Ivins, E.R., Richter, A., Ben Mansour, W., Magnani, M.B., Marderwald, E., Adaros, R., Barrientos, S., 2022. Lithospheric Erosion in the Patagonian Slab Window and Implications for Glacial Isostasy. Geophy. Res. Lett. 49, e2021GL096863.

Meighan, H.E., Pulliam, J., ten Brink, U., López-Venegas, A.M., 2013. Seismic evidence for a slab tear at the Puerto Rico Trench. J. Geophys. Res. 118, 2915–2923.

Millen, D.W., Hamburger, M.W., 1998. Seismological evidence for tearing of the Pacific plate at the northern termination of the Tonga subduction zone. Geology 26, 659–662.

Miller, M.S., Gorbatov, A., Kennett, B.L.N., 2006. Three-dimensional visualization of a near-vertical slab tear beneath the southern Mariana arc. Geochem. Geophys. Geosyst. 7.

Moreno, M., Bolte, J., Klotz, J., Melnick, D., 2009. Impact of megathrust geometry on inversion of coseismic slip from geodetic data: Application to the 1960 Chile earthquake. Geophy. Res. Lett. 36, L16310.

Mpodozis, C., Hervé, M., Nassi, C., Soffia, J., Forsythe, R., Nelson, E., 1985. El magmatismo plioceno de Península Tres Montes y su relación con la evolución del Punto Triple de Chile Austral. Rev. Geol. Chile 25-26, 13–28.

Murdie, R., Prior, D., Styles, P., Flint, S., Pearce, R., Agar, S., 1993. Seismic responses to ridge-transform subduction: Chile triple junction. Geology 21, 1095–1098.

Murdie, R., Russo, R., 1999. Seismic anisotropy in the region of the Chile Margin Triple Junction. J. South Am. Earth Sci. 12, 261–270.

Murdie, R., Styles, P., Prior, D., Daniel, A., 2000. A new gravity map of southern Chile and its preliminary interpretation. Rev. Geol. Chile 27, 49–63.

Notsu, K., Lopez-Escobar, L., Onuma, N., 1987. Along-arc variation of Sr-isotope composition in volcanic rocks from the Southern Andes (33°S-55°S). Geochemical Journal 21, 307–313.

Pallares, C., Maury, R., Bellon, H., Royer, J.Y., Calmus, T., Aguillo-Robles, A., Cotten, J., Benoit, M., Michaud, F., Bourgois, J., 2007. Slab-tearing following ridge-trench collision: Evidence from Miocene volcanism in Baja California, Mexico. J. Vol. Geo. Res. 161, 95–117.

Portner, D.E., Beck, S., Zandt, G., Scire, A., 2017. The nature of subslab slow velocity anomalies beneath South America. Geophy. Res. Lett. 44, 4747–4755.

Priestley, K., Tilmann, F., 2009. Relationship between the upper mantle high velocity seismic lid and the continental lithosphere. Lithos 109, 112–124.

Ramos, V., 2005. Seismic ridge subduction and topography: Foreland deformation in the Patagonian Andes. Tectonophysics 399, 73–86.

Ramos, V., Kay, S., 1992. Southern Patagonian plateau basalts and deformation: backarc testimony of ridge collision. Tectonophysics 205, 261–282.

Rodriguez, E., Russo, R., 2019. Southern Chile crustal structure from teleseismic receiver functions: Responses to ridge subduction and terrane assembly of Patagonia. Geosphere 16, 378–391.

Ruiz, S., Madariaga, R., 2018. Historical and recent large megathrust earthquakes in Chile. Tectonophysics 733, 37–56.

Russo, R.M., VanDecar, J., Comte, D., Mocanu, V., Gallego, A., Murdie, R., 2010. Subduction of the Chile Ridge: Upper mantle structure and flow. GSA Today 20, 4–10.

Sáez, M., Ruiz, S., Ide, S., Sugioka, H., 2019. Shallow Nonvolcanic Tremor Activity and Potential Repeating Earthquakes in the Chile Triple Junction: Seismic Evidence of the Subduction of the Active Nazca–Antarctic Spreading Center. Seismol. Res. Lett. 90, 1740–1747.

Scales, J., 1987. Tomographic inversion via the conjugate gradient method. Geophysics 52, 179–185.

Scherwath, M., Contreras-Reyes, E., Flueh, E., Grevemeyer, I., Krabbenhoeft, A., Papenberg, C., Petersen, C., Weinrebe, R., 2009. Deep lithospheric structures along the southern central Chile margin from wide-angle P-wave modelling. Geophys. J. Int. 179, 579–600.

Seton, M., Müller, R.D., Zahirovic, S., Williams, S., Wright, N.M., Cannon, J., Whittaker, J.M., Matthews, K.J., McGirr, R., 2020. A Global Data Set of Present-Day Oceanic Crustal Age and Seafloor Spreading Parameters. Geochem. Geophys. Geosyst. 21, e2020GC009214.

Siebert, L., Simkin, T., 2002. Volcanoes of the World: an Illustrated Catalog of Holocene Volcanoes and their Eruptions. Smithsonian Institution, Global Volcanism Program, Digital Information Series, GVP-3 Http://www.volcano.si.edu/world/.

Stern, C., 2004. Active Andean Volcanism: its geologic and tectonic setting. Rev. Geol. Chile 31, 161–206.

Stern, C., 2008. Holocene tephrochronology record of large explosive eruptions in the southernmost Patagonian Andes. B. Volcanol. 70, 435–454.

Suárez, M., de la Cruz, R., Bell, C., 2000. Timing and origin of deformation along the Patagonian fold and thrust belt. Geological Magazine 137, 345–353.

Tassara, A., 2010. Control of forearc density structure on megathrust shear strength along the Chilean subduction zone. Tectonophysics 495, 34–47.

Thorkelsen, D., 1996. Subduction of diverging plates and the principles of slab window formation. Tectonophysics 255, 47–63.

Thorkelson, D., Breitsprecher, K., 2005. Partial melting of slab window margins: genesis of adakitic and non-adakitic magmas. Lithos 79, 25–41.

Tilmann, F., Benz, H., Priestley, K., Okubo, P., 2001. P-wave velocity structure of the uppermost mantle beneath Hawaii from traveltime tomography. Geophys. J. Int. 146, 594–606.

VanDecar, J., 1991. Upper-mantle structure of the Cascadia Subduction Zone from non-linear teleseismic travel-time inversion. PhD thesis, University of Washington, Seattle .

VanDecar, J., Crosson, R., 1990. Determination of teleseismic relative phase arrival times using multi-channel cross correlation and least squares. B. Seismol. Soc. Am. 80, 150–169.

Veloso, E., Anma, R., Ota, T., Komiya, T., Kagashima, S., Yamazaki, T., 2007. Paleocurrent patterns of the sedimentary sequence of the Taitao ophiolite constrained by anisotropy of magnetic susceptibility and paleomagnetic analyses. Sedimentary Geology 201, 446–460.

Veloso, E., Anma, R., Yamazaki, T., ., 2005. Tectonic rotations during Chile Ridge collision and obduction of the Taitao ophiolite (southern Chile). The Island Arc 14, 599–615.

Villar-Muñoz, L., Kinoshita, M., Bento, J.P., Vargas-Cordero, I., Contreras-Reyes, E., Tinivella, U., Giustiniani, M., Abe, N., Anma, R., Orihashi, Y., Iwamori, H., Nishikawa, T., Veloso, E.A., Haraguchi, S., 2021. A cold seep triggered by a hot ridge subduction. Scientific Reports 11, 20923.

Wang, K., Hu, Y., Bevis, M., Kendrick, E., Vargas, R., Lauria, E., 2007. Crustal motion in the zone of the 1960 Chile earthquake: Detangling earthquake-cycle deformation and forearc-sliver translation. Geochem. Geophys. Geosyst. 8, Q10010.

Wessel, P., Smith, W.H.F., Scharroo, R., Luis, J., Wobbe, F., 2013. Generic Mapping Tools: Improved Version Released. EOS Trans. AGU 94, 409–

410.

Wortel, M., Vlaar, N., 1978. Age-dependent subduction of oceanic lithosphere beneath western South America. Phys. Earth Planet. In. 17, 201–208.

Zhao, D., Hasegawa, A., Horiuchi, S., 1992. Tomographic imaging of P and S wave velocity structure beneath northeast Japan. J. Geophys. Res. 97, 19909–19928.

Supplementary Material: *P*-wave teleseismic tomography of the subducted Chile Rise

Matthew Miller[a,*], Keith Priestley[b], Frederik Tilmann[c,d], Klaus Bataille[e], Hikaru Iwamori[f]

[a]*Departamento de Geofísica, Universidad de Concepción, Concepción, Chile*
[b]*Department of Earth Sciences, Bullard Laboratories, University of Cambridge, Cambridge, United Kingdom*
[c]*Department of Geophysics, Deutsches GeoForschungsZentrum GFZ, Potsdam, Germany*
[d]*Department of Earth Sciences, Institute of Geological Sciences, Freie Universität Berlin, Berlin, Germany*
[e]*Departamento de Ciencias de la Tierra, Universidad de Concepción, Concepción, Chile*
[f]*Earthquake Research Institute, University of Tokyo, 1-1-1, Yayoi, Bunkyo-ku, Tokyo, 113-0032, Japan*

S1. Data Set Correlations

Figure S1 shows the correlation coefficients calculated as a function of station separation for the entire data set. The distance between the stations has only a small effect on how well-correlated the traces are, justifying the filter and window values described in Section 2.2.
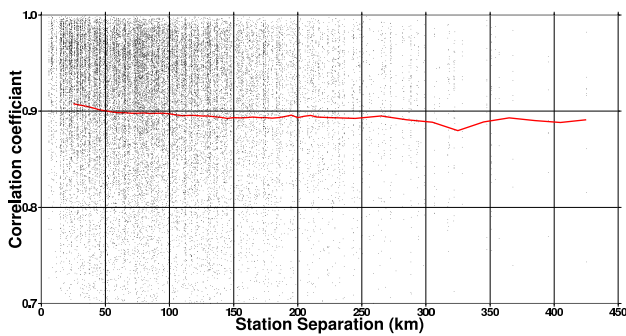
Figure S1: The correlation coefficients as a function of the distance between the station pairs for all used *P* events. The red line indicates a running mean with a sample window of 50 km.

S2. Model Node Selection

The total number of nodes used in the inversion was 63,945. The grid spacing was chosen so as to not limit the resolution of the tomographic image. The 29 nodes in depth extend from sea level to 400 km, with 5 km spacing for the top 30 km, 10 km spacing for the next 70 km, and 20 km spacing for the next 300 km. In latitude, the 49 nodes are spaced every 0.1° from 45°S to 48°S, every 0.2° out to 44°S and 49°S, and every 0.5° out to 42°S and 51°S. In longitude, the 45 nodes are spaced 0.1° 71°W to 74°W, every 0.2° out to 70°W and 75°W, and every 0.5° out to 69°W and 76°W. The inversion nodes are dependent on their neighbors, as they are constrained by model smoothing and flattening constraints detailed in Section S3, and consequently the inversion is stable. Figure S2 displays the positions of the nodes relative to the study area. It should be noted that the large amount of nodes at shallow depths of less than 30 km, put in to allow more accurate ray tracing near the surface, are probably superfluous and unnecessarily increase the inversion time. The shallowest nodes do not show velocity variations from the inversion, as the station terms account for the shallow structure.
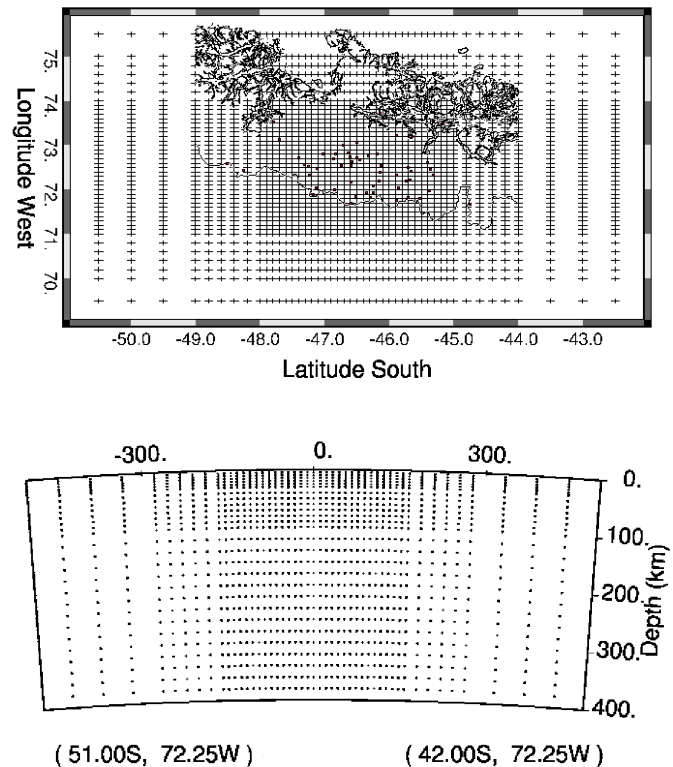

Figure S2: The nodes used to define the slowness model. The squares indicate the stations of the network used in this study. The scale of the vertical cross-section is in kilometers. The coastline and Chile-Argentina border are included for reference.

---

*Corresponding Author: mrmiller@udec.cl

S3. Choice of Inversion Parameters

Following **?**, the hypocenter perturbation damping was set to 0.0025 km^{-1}, the station term damping set to 10 s^{-1} and the ratio between the flattening and smoothing constraints was taken to be 20 (other values from 5 to 100 were also tested). Concerning the hypocenter perturbations, small errors in hypocentral location far from the networks can produce small deviations in the expected backazimuth and incidence angle of the rays arriving at the network. In the inversion, these perturbations were up to 5 km in the horizontal direction, and 1 km vertically: such small values are expected from the well-located hypocenters used in this study and have a negligible effect on the inversion.

The optimal value for the flattening parameter needs to be calculated for this particular data set. If the flattening parameter is set too high, the output slowness model will not have sufficient spatial variation or magnitude to match the traveltime anomalies; if the flattening parameter is too low then the output slowness model will show a large variation on short length scales, essentially fitting the noise in the data.

In order to determine the optimum flattening parameter needed in this inversion the *P*-wave data set was split randomly into two halves. The inversion procedure was then applied to the two half data sets separately to produce two different tomographic models. The lower the flattening parameter, the more complicated the output slowness model (measured in terms of the root mean squared (RMS) deviation of the percentage slowness anomaly of the slowness model nodes, weighted by ray density), and the better the fit between the model and the half data set that was used to produce it (measured in terms of the RMS deviation from the traveltimes predicted from the final model and the actual traveltimes). Finally, the rays from the half of the dataset not used to generate the tomography model had their predicted traveltime residuals calculated using the model generated by the other half of the data set, and the RMS deviation calculated. This procedure was repeated five times to provide ten half-data sets, and a wide range of flattening parameters used, the results of which are displayed in Figure S3. The ideal flattening parameter is at the minimum in the curve showing the RMS deviation of the traveltimes of the second half of the data set with the predicted traveltimes of these rays using the slowness model generated by the first half (red line). It is reassuring to note that this flattening parameter reduces the standard deviation of the traveltime residuals to 0.08 s, the calculated picking error of the MCCC procedure. Within the error shown by the one standard deviation bars marked on the plots, the range of flattening parameters that could be used is large, due to the low curvature of this minimum. Several flattening parameters within the acceptable range were tested and the robust features in the tomography model were consistent for these inversions. The chosen flattening and smoothing parameters used in this study were 0.5 km^{2}s^{-1} and 10 km^{3}s^{-1} respectively.
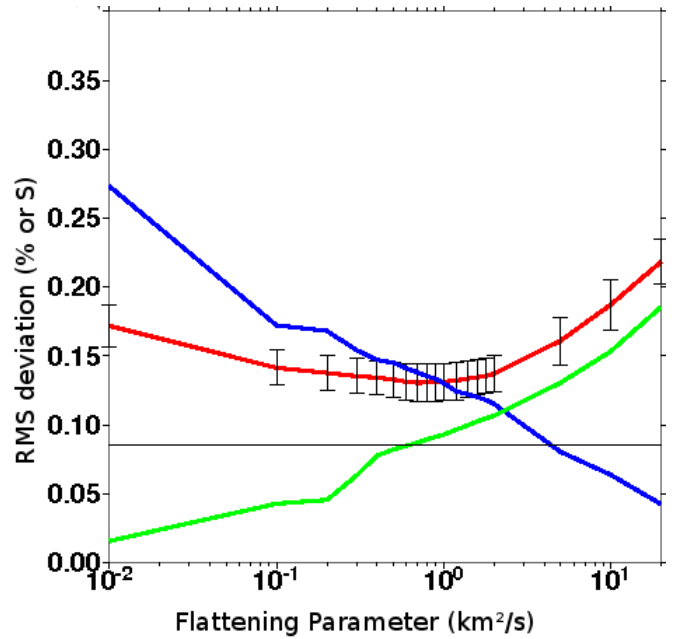

Figure S3: The results of the test to determine the optimal flattening parameter for the tomographic inversion. The data is the average of 10 half data sets, and has the flattening parameter on the x-axis. Blue line: RMS deviation of the percentage slowness anomaly of the slowness model nodes, weighted by ray density. Green line: RMS deviation in seconds from the traveltimes predicted from the final model and the actual traveltimes, for the half of the data used to generate the model. Red line: RMS deviation in seconds from the traveltimes of the second half of the data set with the predicted traveltimes of these rays using the slowness model generated by the first half of the data set; the error bars displayed are one standard deviation from the average value. Black horizontal line: The estimated picking error in seconds made by comparing the relative traveltimes from different events originating in roughly the same location. The initial RMS value of the travel times was 0.33 s.

S4. Additional Checkerboard Resolution Tests

Additional checkerboard resolution tests are displayed in Figure S4 to permit a reader to see a wider range of structures, and the inversion of the theoretical traveltimes that they produce. As mentioned in the main text, Gaussian noise representative of the traveltime uncertainty is added to the synthetic data to mimic the challenge that the inversion faces; without this noise the recovery of the synthetics is noticeably better. The smallest block size, 0.35° x 0.35° x 40 km, shown in Figures S4(a) and S4(b), is considered unresolved.
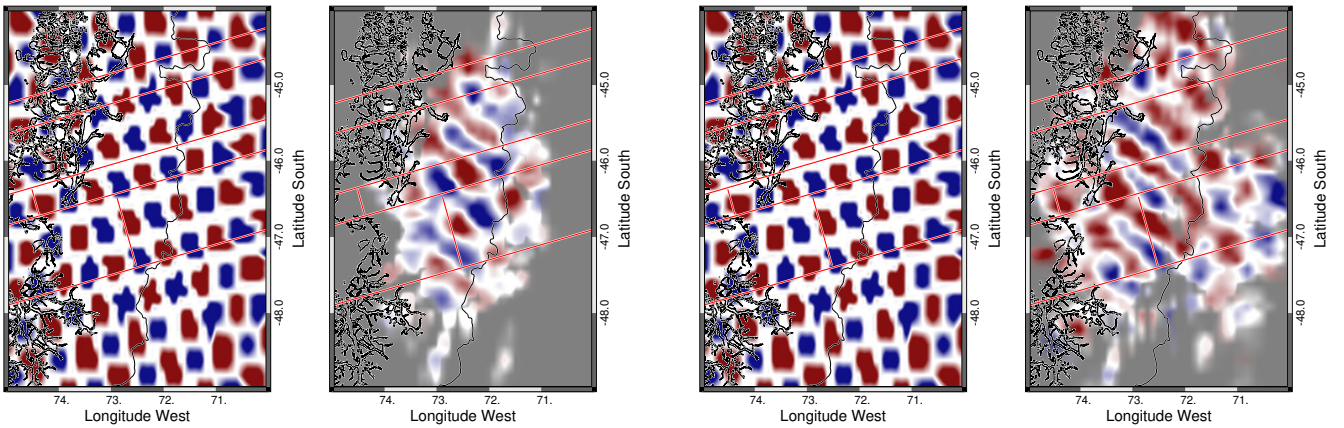
References

Tilmann, F., Benz, H., Priestley, K., Okubo, P., 2001. *P*-wave velocity structure of the uppermost mantle beneath Hawaii from traveltime tomography. Geophys. J. Int. 146, 594–606.
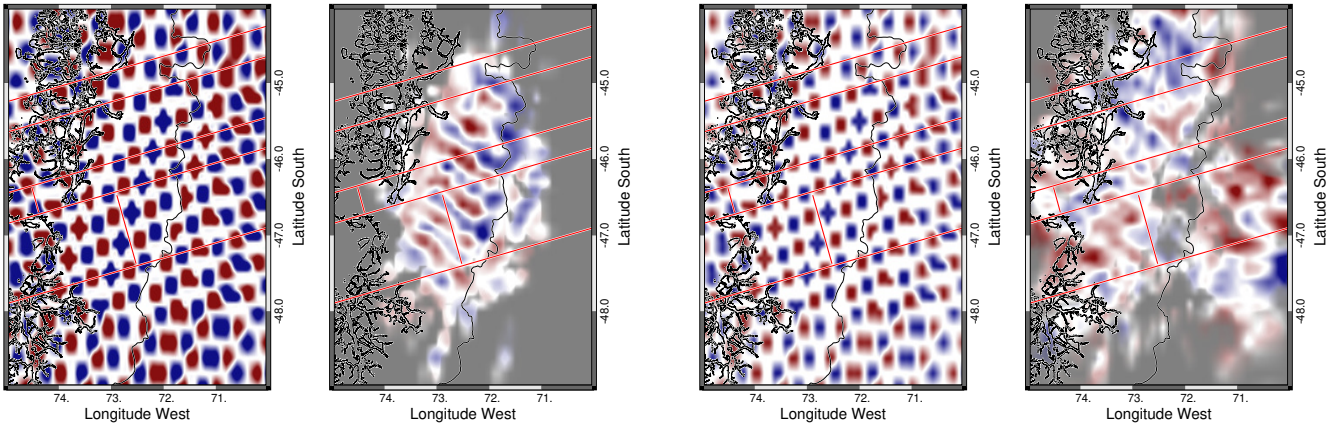
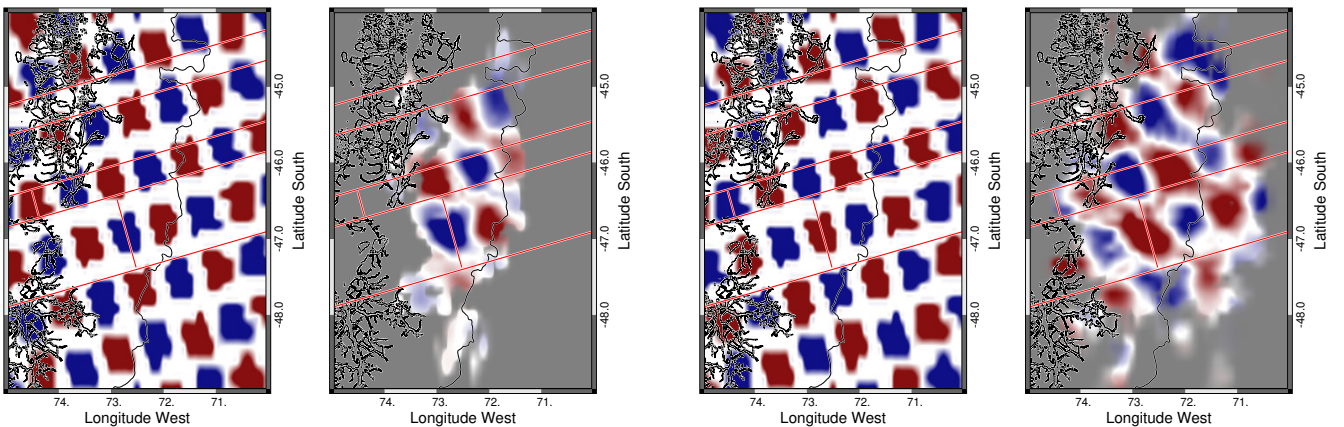(a) Block size ~40km, depth = 100 km, input and inversion

(b) Block size ~40km, depth = 250 km, input and inversion

(c) Block size ~60km, depth = 100 km, input and inversion

(d) Block size ~60km, depth = 200 km, input and inversion

(e) Block size ~90km, depth = 50 km, input and inversion
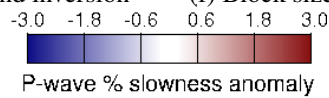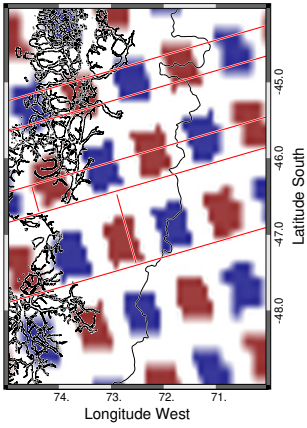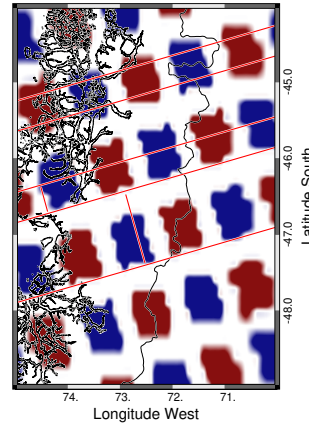
(f) Block size ~90km, depth = 150 km, input and inversion

-3.0 -1.8 -0.6   0.6   1.8   3.0

P-wave % slowness anomaly

Figure S4: Checkerboard resolution tests, depth slices. The slowness anomaly is presented as a percentage deviation from the reference IASP91 velocity model. Areas of low ray coverage, less than 0.01 km^{-2}, are shown with reduced brightness at the edge of the illuminated region and areas with ray coverage lower than 0.001 km^{-2} are covered in gray. Of each pair, on the left are the original synthetic slowness models and on the right are the reproduced models by the inversion. Depths are chosen to show slices that cut close to the centers of the synthetic blocks.

(g) Block size ~120km, depth = 150 km, input and inversion

(h) Block size ~120km, depth = 300 km, input and inversion
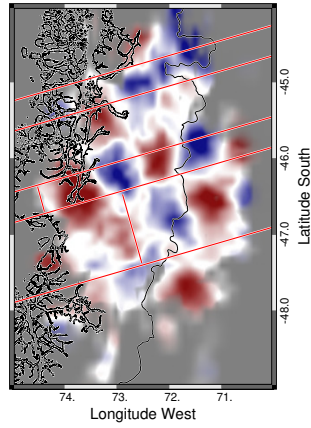
(i) Block size ~200km, depth = 100 km, input and inversion
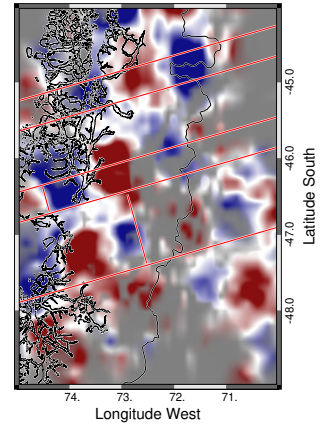
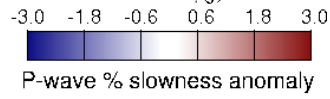(j) Block size ~200km, depth = 250 km, input and inversion

P-wave % slowness anomaly

Figure S4: Continued.

S4